

An Effective Method of Weld Defect Detection and Classification Based on Machine Vision

Jun Sun , *Member, IEEE*, Chao Li, Xiao-Jun Wu, Vasile Palade, *Senior Member, IEEE*, and Wei Fang, *Member, IEEE*

Abstract—In order to effectively identify and classify weld defects of thin-walled metal canisters, a weld defect detection and classification algorithm based on machine vision is proposed in this paper. With the weld defects categorized, a modified background subtraction method based on Gaussian mixture models, is proposed to extract the feature areas of the weld defects. Then, we design an algorithm for weld detection and classification according to the extracted features. Next, by using the weld images sampled by the constructed weld defect detection system on a real-world production line, the parameters of the weld defect classifiers are determined empirically. Experimental results show that the proposed methods can identify and classify the weld defects with more than 95% accuracy rate. Moreover, the weld detection results obtained in the actual production line show that the detection and classification accuracy can reach more than 99%, which means that the system enhanced with the proposed method can meet the requirements for the best real-time and continuous weld defect detection systems available nowadays.

Index Terms—Gaussian mixture models, machine vision, weld defect classification, weld defect detection.

I. INTRODUCTION

IN METAL packaging industry, factories manufacture metal cans through standardized production lines [1], and most of the production technology in the canister production is mature and of high degree of automation. In welding seam inspection, the X-ray flaw detection is a widely used technology and it mostly applied for thick metal workpieces, such as thick steel pipes since it employ X-ray penetration to detect the interior flaws of welding seams [2]–[6]. X-ray flaw detection is

essentially a machine vision-based technology, but it is not suitable for welding inspection of thin-walled metal canisters for the following reasons. First, electric resistance welding, which is very different from electric welding method for thick metal workpieces, is used for thin-walled metal canisters, and there are no welding porosities and slags in the interior of welding seams of the workpieces. Second, for thin-walled metal canisters, the welding seams are thin enough so that the welding flaws or defects are generally visible and there is no need of using X-ray penetration for interior flaw detection. Other machine vision methods have also been employed for the weld defect detection, but all of these methods are also just suitable for thick-walled metal workpieces and cannot be applied directly for thin-walled ones due to different features of weld seams [7]–[9]. As such, the most commonly employed weld defect detection method for thin-walled metal canisters is still the human visual detection, which has many disadvantages [10]. For the purpose of automatizing the weld seam defect detection process in the actual production, we propose a real-time weld detection approach based on machine vision and designed the corresponding system for thin-walled metal canister production lines. The system takes gray images of the weld seams on the production line by using an industrial camera at very short time intervals, and then detects the weld seam images and pushes off the defective cans from the production line immediately.

The core part of the system is of course the weld defect detection algorithm. Except the time intervals, the image sequence obtained by the camera is similar to the successive image frames in a video, so that the moving target detection and segmentation method, which is widely applied in the detection of moving objects in video, can be used for the detection purpose. The existing methods of moving target detection can be divided into three categories: optical flow methods, interframe difference methods and background subtraction methods. Optical flow methods are very sensitive to noise and need a large amount of calculation [11], [12], so that they are not suitable for real-time requirements of the production lines. Interframe difference techniques are sensitive to light variation, and sometimes they are unable to extract moving targets completely which may have empty areas inside [13], [14]. Background subtraction approaches, the most widely employed ones, are used in our systems since they can provide the complete features of the moving target in most cases [15]–[18]. This method is usually implemented through two steps: Construction and the updating of the background model [15].

Manuscript received October 29, 2018; accepted January 7, 2019. Date of publication January 30, 2019; date of current version December 3, 2019. This work was supported in part by the National Natural Science Foundation of China under Grant 61673194, Grant 61672263, Grant 61672265, and Grant 61876072; and in part by the National First-Class Discipline Program of Light Industry Technology and Engineering under Grant LITE2018-25. Paper no. TII-18-2830. (Corresponding author: Jun Sun.)

J. Sun, C. Li, X.-J. Wu, and W. Fang are with the Jiangsu Provincial Engineering Laboratory of Pattern Recognition and Computational Intelligence, Jiangnan University, Wuxi 214122, China (e-mail: sunjun_wx@hotmail.com; chao.li-jn@hotmail.com; wu_xiaojun@jiangnan.edu.cn; wxfangwei@hotmail.com).

V. Palade is with the Faculty of Engineering, Environment and Computing at Coventry University, Coventry CV1 5FB, U.K. (e-mail: ab5839@coventry.ac.uk).

Color versions of one or more of the figures in this paper are available online at <http://ieeexplore.ieee.org>.

Digital Object Identifier 10.1109/TII.2019.2896357

However, the background subtraction algorithm needs to compare each pixel of the current input image with that of the background image, thus having the following two major shortcomings [17]. One is that the gray values of the foreground and the background of the image should have a certain degree of difference; otherwise, the recognition rate of the algorithm would be reduced. The other is that the method is too sensitive to environmental changes, for example, changes in illumination. Thus, it is necessary to ensure that the sampling environment is consistent when the algorithm is employed. In order to solve such problems, a lot of work has been done on improving the method [19]–[22]. For example, Wren *et al.* proposed a single Gaussian (SG) method to model the background [19]. Stauffer and Grimson designed a Gaussian mixture model to express and construct a complex background [20]. Elgammal *et al.* used kernel density estimation (KDE) algorithm to distinguish the foreground from the background [21]. In [22], subspace learning using PCA was proposed to construct the background. Each of these methods has its own advantages and limitations, and their effectiveness depends on the characteristics of practical problems.

In this paper, we proposed a real-time online weld defect detection method for the thin-walled metal canisters production and developed the corresponding detection system for actual production line. Our work has the following contributions. First, based on Stauffer's work [20], we propose a modified background subtraction (MBS) algorithm, which regards the normal welding seam as the background and the welding seam defect as the foreground. This algorithm constructs a mixture model containing two Gaussian models, and the way of updating their parameters is different from the one proposed by Stauffer. When the MBS is made, the defect areas are thus extracted. By comparing these defect areas, we can find that different types of welding seam defects have different features, by which weld defects can be identified and classified by the system with high accuracy. In our method, the MBS algorithm is first implemented to construct the background of image sequence and extract the defect areas, and then the weld defect classification algorithm is employed to distinguish the types of weld defects according to the features of defects. Particularly, for our classification algorithm, we propose a gray-value curve method for distinguishing weld fusions from weld perforations. This feature extraction method is first proposed in this paper and is showed to be very effective and efficient in real-time welding defect detection for the thin-walled metal canister production.

The rest of this paper is structured as follows. In Section II, various types of weld defects of thin-walled metal canisters are discussed. Section III presents the proposed MBS algorithm and Section IV describes the proposed weld defect detection and classification algorithm. The experimental results and discussions are presented in Section V. Finally, the paper is concluded in Section VI.

II. TYPES OF WELD DEFECTS

There are many kinds of defects in the welding seam of thin-walled metal canisters, most of which are due to the



Fig. 1. Normal welding seam.

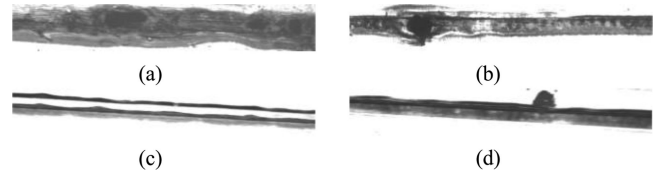


Fig. 2. (a) Weld fusion. (b) Weld perforation. (c) Cold solder joint. (d) Pseudodefekt.

shortcomings of the welding process and the characteristics of the metal. In the metal canning industry, high frequency resistance welding technology is widely applied in welding thin-walled metal canisters. Fig. 1 shows a picture of the normal weld on a metal canister. In the figure, the black area is the welding seam of metal canisters, namely the weld area, and the white area above and below the weld area is known as the blank area. Thin-walled metal canisters are prone to yield defects because of the change in welding current, the instability of electrode pressure as well as some other reasons. Referring to the relevant literature [23]–[26] and combining the actual production conditions for thin-wall workpieces, we categorize weld defects into the following types after carrying out some preliminary statistics.

The first type of defects are known as weld fusions and are usually caused by the excessively high temperature around the electrode, which is always resulted from nonmatching welding speed or slow rotation of the wheel. The area of such a defect, as shown in Fig. 2(a), is usually larger than that of other types and always covers most of the image. The second type is weld perforation. Such a defect is usually caused by ink, paint, and other pollutants in the welding area. These pollutants can increase the welding current, thus making the metal surface broken down. Moreover, around the weld perforation area, there is generally a small amount of weld fusion because of the uneven heating. Fig. 2(b) shows that this kind of defects appears as circular holes with low brightness. Another type is cold solder joint, usually due to the low pressure of the roller electrode or the low electric current in the process of welding, which makes the welding temperature lower than the melting temperature so that the joint fails to reach the melting state. It is shown in Fig. 2(c) that such a defect appears as an area brighter than normal areas.

Besides, in the complex weld production environment, a mixture of dust and rust proof glue may fall onto the weld area because of vibration. In the sample images, these impurities appear as small pieces of black areas and yield the so-called pseudodefects as shown in Fig. 2(d). This kind of defects may result in false detection, if we fail to deal with them properly. There are still a few other types of weld defects not discussed here as they have no obvious visual features on the surface.

III. PROPOSED METHOD

A. Motivation and Principle of the Proposed Method

As mentioned in the introduction, employing a background subtraction algorithm should overcome the two major shortcomings. Specifically, when the algorithm is used for the weld defect detection, it is required that there should be clear difference between the foreground target and the background image and that the difference in background environments between samples should be as small as possible. For the first condition, by investigating a large number of samples, we summarize several features from the image sequence of the samples as follows:

- 1) the shapes of the weld areas are slightly inclined rectangles;
- 2) in the same batch of images, the angles of inclinations are almost the same;
- 3) the features of normal weld images are basically stable, and the boundaries of the weld area are fairly smooth;
- 4) generally, the main area of a normal weld image is a completely connected weld area, not divided into several weld areas; and
- 5) for a defective weld, there are significant differences of texture in the interior or on both sides of the weld areas compared with normal welds.

According to these features and the theory of Stauffer and Grimson [20] and Zivkovic [27], the whole normal weld image can be considered as the background. Since there is significant difference between the weld areas and the blank areas, the background is initialized to a Gaussian mixture model consisting of two Gaussian models. The defect areas in the defected weld images can be regarded as the foreground, which is analogous to the moving targets of background subtraction. It is obvious that this analogy makes the first condition met.

For the second requirement, it is found that in actual production, the features of the weld images are different mainly because of the difference between different batches of products. For example, a small change in the diameters of the metal canisters leads to the change in shooting distance; a change in the placing angle of the metal canisters causes the variation of the imaging area. Nevertheless, for the same batch of products, the features of the weld images shot in a continuous time interval are basically stable. Thus, if there are large differences between different batches, new background models should be constructed; otherwise, the background model keeps unchanged. This method cannot only meet the second requirement, but can also guarantee the algorithmic efficiency.

Based on the earlier discussions, the procedure of MBS algorithm is described as follows.

- 1) For the weld sequence of the same batch, the gray level of each point is chosen according to certain rules to construct the background model.
- 2) Subtract the background model from each image so that the features of the weld defects can be extracted.
- 3) The background model should be reconstructed if the result is beyond the given threshold, in order to ensure the background model to be updated duly.

In the rest of this section, the three steps in the MBS method will be described in detail.

B. Construction of the Background Model

When the background model is constructed, each pixel in the background model is expressed by a Gaussian mixture model [28]–[30]. In this paper, the linear interpolation method is employed to update the mean and the standard deviation of the Gaussian model. Such a method can avoid the dependence of algorithm on the selection of the initial values as well as improving the speed of the algorithm implementation. The background model is constructed through the three steps below.

1) Defining and Initializing the Parameters of the Gaussian Mixture Model: The Gaussian mixture model contains two Gaussian models $G_1(\theta_1)$ and $G_2(\theta_2)$, where $\theta_1 = (\mu_1, \sigma_1, \phi_1)$ and $\theta_2 = (\mu_2, \sigma_2, \phi_2)$ correspond to parameter vectors of the weld area and the blank area of the image, respectively. Here, μ_1 and μ_2 denotes the cluster centers, σ_1 and σ_2 represent the cluster distances, i.e., the standard deviations of the Gaussian models, and ϕ_1 and ϕ_2 are known as the weight factors.

A general method of initializing the Gaussian mixture model is to give a priori initial values on the basis of the experience. However, this initialization method has poor stability. Besides, since there properly are great differences in the welds between different batches of canisters, it is difficult to find a suitable initial value according to the experience. In addition, as mentioned in the following section, the difference in the welds is little in the same batch. Thus, in this paper, we propose a background initialization method with the following steps.

Step 1: Randomly select an image from the image sequences of the same batch.

Step 2: Use the Otsu method [31] to segment the image into the weld area from the blank area of the image, and the two Gaussian models in the Gaussian mixture model are initialized by these two areas, respectively. Given that the threshold obtained by the Otsu method is T , the pixels with their gray values smaller than or equal to T constitute the weld area I_1 and those with the gray values larger than T constitute the blank area I_2 .

Step 3: Calculate μ_{10} and μ_{20} , the initial mean values of I_1 and I_2 , σ_{10} and σ_{20} , and the initial standard deviation of I_1 and I_2 .

Step 4: Initialize the weight factors as $\phi_{10} = 1$ and $\phi_{20} = 1$.

Through the above steps, the parameters of the two Gaussian models in the Gaussian mixture model can be initialized as $\theta_{10} = (\mu_{10}, \sigma_{10}, \phi_{10})$ and $\theta_{20} = (\mu_{20}, \sigma_{20}, \phi_{20})$.

2) Training the Model by the Shooting Samples and Using a Linear Interpolation Method to Update the Mean Values, Standard Deviation and Weight Factors: After the background model initialization, the model should be trained by each sample in the image sequence one by one. Let $f(x, y)$ represents the gray level value of the input image at pixel (x, y) , which is used to update the parameters at the corresponding pixel in background model. To be more specific, with the given $f(x, y)$ in the two Gaussian

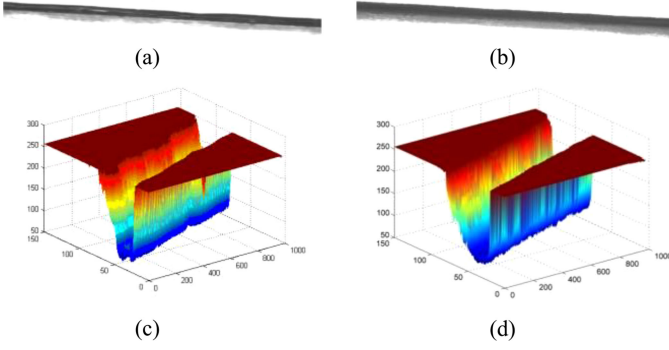


Fig. 3. (a) One frame of a weld image sequence. (b) Background model of the same image. (c) 3-D view of figure (a). (d) 3-D view of figure (b).

models, $N_i(f; \mu_i, \sigma_i)$, $i = 1, 2$ can be calculated by

$$N_i(f; \mu_i, \sigma_i) = \exp \left\{ \frac{-(f(x, y) - \mu_i)^2}{2\sigma_i^2} \right\}, i = 1, 2 \quad (1)$$

and then compared to determine which cluster center pixel (x, y) belongs to. If pixel (x, y) belongs to $G_i(\mu_i, \sigma_i, \phi_i)$, $i = 1, 2$, the mean values, standard deviation and weight factors of θ_i can be updated by

$$\begin{aligned} \mu_i &= \frac{\phi_i \mu_i + f(x, y)}{\phi_i + 1} \\ \sigma_i &= \frac{\phi_i \sigma_i + |f(x, y) - \mu_i|}{\phi_i + 1} \\ \phi_i &= \phi_i + 1. \end{aligned} \quad (2)$$

For each pixel in each training sample, the earlier procedure should be repeated to update the parameters of the corresponding Gaussian mixture model of the background, until the parameters of each model are stable. Typically, let δ represent the average change ratio of all μ_i . When $|\delta| < \varepsilon$, the parameter is regarded to be stable. In this paper, we set the threshold $\varepsilon = 10^{-3}$ in an empirical way, which was shown by experimental results to be able to meet the requirement of background construction for weld defect detection.

3) Comparing the Weight Factors of the Two Gaussian Models at Each Pixel, and Selecting the Corresponding Mean Value as the Pixel Value in the Background Model: After the parameters tend to be stable, the weight factors of the two Gaussian models at each pixel should be compared. It is hypothesized that the mean value of the Gaussian model with higher weight factor is chosen as the gray value at the pixel.

Through the above three steps, the background model of metal canister welds in the same batch can be constructed. For example, Fig. 3(a) is the image of a normal weld in an image sequence, and Fig. 3(b) is the background model of the same image sequence, which is constructed by the earlier algorithm after 40 iterations. From the corresponding three-dimensional (3-D) views in Fig. 3(c) and (d), we can see that the edge of the background model is smoother than the other.

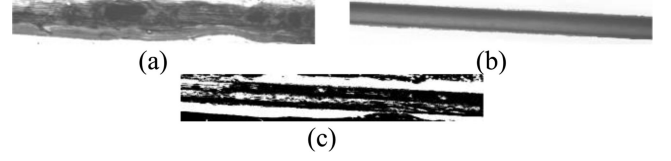


Fig. 4. (a) Defect welding seam. (b) Corresponding background model. (c) Binary image of foreground.

C. Feature Extraction of Weld Defects

When the background model is constructed, the features of the weld defects can be extracted through the following three steps.

1) Making Subtraction Between the Input Image and the Background Image so That the Foreground of the Binary Image Will be Extracted: In a set of consecutively sampled images, we denote the k th frame image as D_k and its corresponding background image as B_k . If the difference between the pixel values at the same position in D_k and B_k is larger than the threshold T , the pixel point is considered as a pixel in the foreground and its value is then set to 1; otherwise, the pixel point corresponds the one in the background and its value is set to be 0. Therefore, the binary image of the foreground, denoted by F_k , can be expressed as

$$F_k(x, y) = \begin{cases} 1, & |D_k(x, y) - B_k(x, y)| \geq T \\ 0, & |D_k(x, y) - B_k(x, y)| < T \end{cases} \quad (3)$$

where T is the threshold. Fig. 4(a) depicts the example of weld fusion presented in Fig. 2(a), and Fig. 4(b) is the background model constructed for the corresponding image sequence which shown in Fig. 4(a). By comparing Figs. 3(b) and 4(b), we can see that the background models of different batches look very different. Fig. 4(c) is the binary image of the foreground made by subtraction.

The threshold T in (3) is generally set in an empirical way. However, considering the uncertainty of the background model, each pixel point has its own threshold T associated with its corresponding Gaussian mixture model. In this paper, the threshold T is set to be a multiple of the standard deviation σ_i , changing with the background model. Preliminary experiments showed that $T = 3\sigma_i$ leads to good segmentations in general.

2) Denoising the Binary Image to Obtain the Weld Defect Area: As the texture of the shot weld area changes constantly and its position may also change slightly due to the vibration of the production line, noise can be generated in the foreground image F_k . In order to avoid false detection, we can either reconstruct the background model for the current sampled image or use the method of mathematical morphology to remove the noise area. Considering the expense of background reconstruction, the second method is used in this paper. Specifically, an opening operation by using 9×9 square structuring elements is carried out to eliminate the noise of a small area. For example, Fig. 5(a) is the opening result of Fig. 4(c).

After the opening operation, most of the noise region has been eliminated, but a small amount of noise area still exists. It was found by many experimental results that the areas smaller than



Fig. 5. (a) Image after opening using 9×9 elements. (b) Image after removing connected areas less than 400.



Fig. 6. Feature image of weld defects.

400 pixel points are mostly yielded by uneven illumination or uneven heating. Thus, in this paper, connected areas smaller than 400 pixel points are considered as noise areas, which should be removed.

3) *Implementing Dot Product Between the Binary Image Matrix and the Original Image Matrix to Obtain the Feature Image of Weld Defects:* The binary image of weld defect areas is not enough to distinguish the type of weld defects from the specific features of defect images. Therefore, the dot product is carried out between binary image F_k and the original image D_k so that we can obtain the feature image of weld defects I_k

$$I_k(x, y) = F_k(x, y) \cdot D_k(x, y). \quad (4)$$

In the feature image of defect areas in Fig. 6, except the weld defect areas, the pixel values of the other areas are all 0, which do not have any effect on classification of weld defects undertaken by the algorithm in Section IV.

D. Updating the Background Model

Due to the difference among the background models of different batches, the background model should be able to automatically update to ensure the stability and accuracy of weld defect detection. Generally, the update algorithm of background models is based on the adaptive adjustment of the model parameters [12]. However, the algorithm can only apply to the situation that the background varies slowly, but cannot to the case that there are great differences among different batches. Another commonly used method is to update the background periodically, i.e., to extract several images to the background after the current background model is exploited for a period of time [30]. However, this method does not apply to the case that it is uncertain when the batch of metal canisters is changed.

In this paper, we use the updating strategy proposed by Haraoglu *et al.* [32]. In this algorithm, the background is considered to have a great change and thus needs updating, if over a threshold proportion (e.g., 60% in this paper) of the pixels in each of the images that resulted from the subtraction between 20 continuously shot images and the background image have differences in gray values. When the background model needs to be updated, the algorithm presented in Section III-C is thus employed again to construct a new background model. This method of updating the background model cannot only adapt to the abrupt change of the background model, but also greatly reduce the model update frequency, thus meeting the requirement for top-spec real-time actual production.



Fig. 7. Feature image of a pseudodefekt.



Fig. 8. (a) Original image of a welding seam. (b) Feature image of weld defects.

IV. CLASSIFICATION ALGORITHMS FOR WELD DEFECTS

A. Detection Algorithm by Defect Areas

After feature extraction for weld defects, the feature areas extracted from the image with pseudodefects are very small in general. Fig. 7 shows the feature areas of Fig. 2(d) which contains pseudodefects. We can see that it is much smaller than the feature areas of genuine weld defects shown in Fig. 6.

In addition, because of the instability of the production environment, vibration and displacement of the metal canister as well as slight variation of the weld width are likely to occur. These may lead to false detections since some small feature areas are properly extracted from a normal weld image. In this paper, we name such false detections as false detection of background subtraction. Fig. 8 illustrates a false detection of background subtraction resulted from slight differences in the weld width.

It should be emphasized that the small defect area discussed here cannot be eliminated by the algorithm for removing small connected areas as described in the following section. First, the defect area discussed in this section is the total area of the defects in a weld image, but not the area of a single connected region. Many experimental results show that the defects with small total areas are mostly pseudodefects or false detections of background subtraction (BS). Second, if the algorithm for removing small connected areas is used to get rid of the false detection areas like in Fig. 8(b), we must increase the criterion of the area (i.e., 400 as indicated in Section III), which lead to false removal of a large number of single defect areas and missing detections as well.

According to the earlier discussion, there are obvious differences in areas between pseudodefects (or false detects of background subtraction) and common weld defects. Thus, the method of classification based on defect areas can be formulated as

$$\text{Flag} = \begin{cases} \text{Pseudo defects or flase defects by BS,} & \text{if } S < T_1 \\ \text{General weld defects,} & \text{if } S \geq T_1 \end{cases} \quad (5)$$

where S denotes the number of pixels in the feature area of the weld defect, and T_1 is the threshold value of defect areas which is generally set to be $T_1 = 1 \times 10^4$ according to our experience. Further discussion on T_1 will be undertook in Section V.

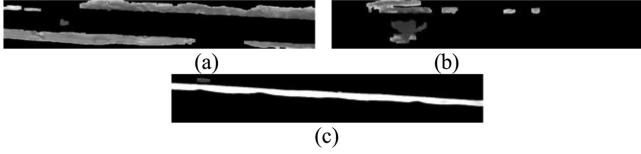


Fig. 9. (a) Feature image of weld fusion. (b) Feature image of weld perforation. (c) Feature image of cold solder joint.

B. Detection Algorithm by Defect Brightness

After pseudodefects and false detection of background subtraction are identified, the three types of genuine weld defects need to be classified. Fig. 9 presents the feature images of the three types of weld defects shown in Fig. 2. It can be observed from the figure that the feature areas of cold solder joint are mainly composed of white areas with high brightness, while the feature areas of the others consist of gray areas with low brightness. Therefore, brightness can be employed to distinguish cold solder joint from the other two types of weld defects. In this paper, the brightness level of the weld defect area is measured by the mean pixel value of the area, which is given by

$$L = \frac{\sum_{i=1}^S X(i)}{S}, (1 \leq i \leq S) \quad (6)$$

where $X(i) (1 \leq i \leq S)$ represents the gray value of each pixel in the defect area and S is the number of the pixels in the area. As such, cold solder joint and other two types of weld defects can be distinguished by

$$\text{Flag} = \begin{cases} \text{Cold solder joint,} & L \geq T_2 \\ \text{Weld fusion and weld perforation,} & L < T_2 \end{cases} \quad (7)$$

where the value of T_2 will be addressed in Section V.

C. Detection Algorithm by Gray-Value Curves

As can be seen from Fig. 9(a) and (b), the feature images of weld fusion and weld perforation show no apparent differences in the brightness and the total areas, but have different regular patterns in the width of defects and edges of the weld area. In this paper, a curve detection algorithm is proposed to distinguish these two types of defects according to the features of their gray-value curves. The algorithm can be implemented through the following three steps.

1) *Summing the Gray Values of the Pixels of Each Column in the Feature Image*: Assuming that the matrix X of the feature image is represented as

$$X = \begin{bmatrix} x_{1,1} & \dots & x_{1,j} & \dots & x_{1,n} \\ \vdots & \ddots & \vdots & \ddots & \vdots \\ x_{i,1} & \dots & x_{i,j} & \dots & x_{i,n} \\ \vdots & \ddots & \vdots & \ddots & \vdots \\ x_{m,1} & \dots & x_{m,j} & \dots & x_{m,n} \end{bmatrix} \quad (8)$$

where $x_{i,j}$ is the gray value of pixel (i, j) ($1 \leq i \leq m, 1 \leq j \leq n$). Then, the sum of gray values in

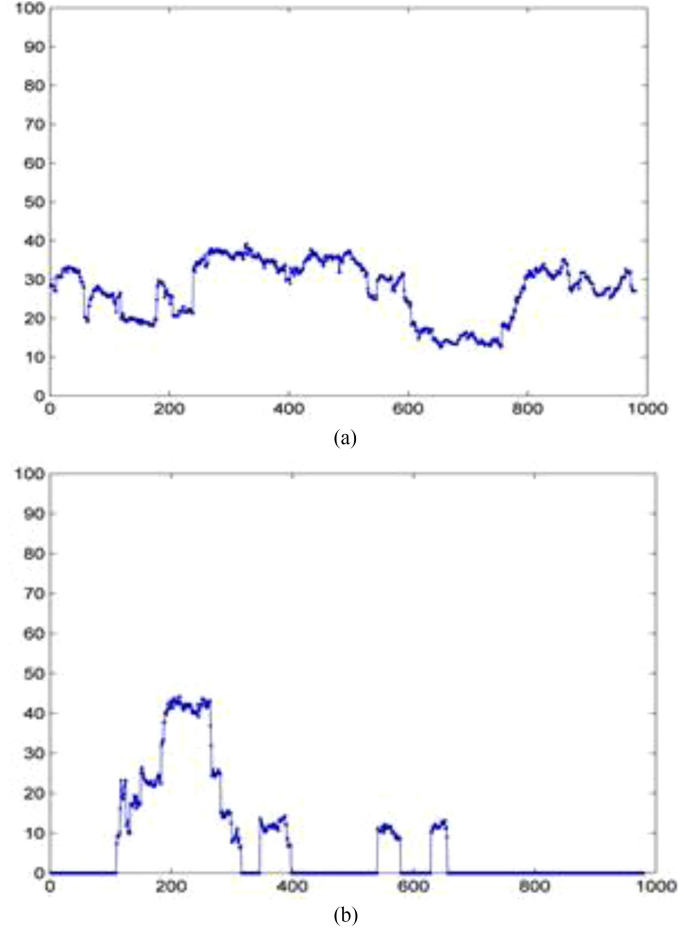


Fig. 10. (a) Gray-value curve of Fig. 9(a). (b) Gray-value curve of Fig. 9(b).

each column is given by

$$s_j = \sum_{i=1}^m x_{i,j} \quad (9)$$

and all s_j 's constitute a row vector

$$S = [s_1, \dots, s_j, \dots, s_n] \quad (10)$$

by which the gray-value curve (also simply called curve) of the feature image can be plotted. Fig. 10 visualizes the curves of Fig. 9(a) and (b).

2) *Curve Smoothing*: Fig. 10 shows a case in which the large fluctuation of the gray values occurs at some adjacent pixel points. Sudden changes in the gray value, which may be caused by noises though, can interfere with our judgment of weld defects based on first-order difference of gray values as will be described in the next step. The resulting misjudgment in weld defect classification may be made. Thus, in this paper, mean filtering is performed to smooth the gray-value curve so that the noise points in the curve can be removed

$$SS(j) = \frac{S(i-mm) + \dots + S(j) + \dots + S(i+mm)}{\text{span}}, \quad mm = (\text{span} - 1) / 2, \quad (11)$$

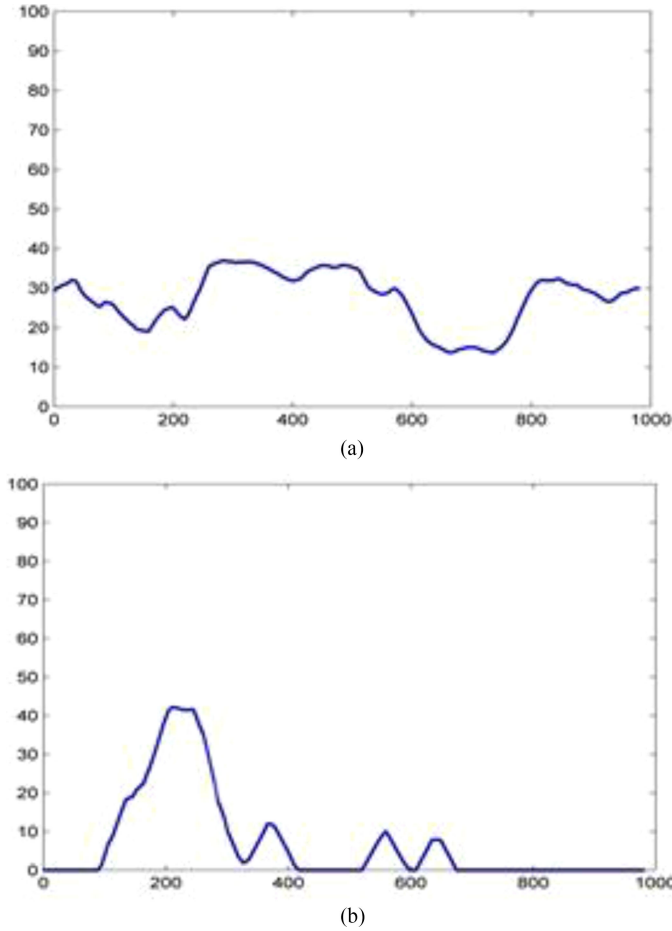


Fig. 11. (a) Smoothed curve of Fig. 11(a). (b) Smoothed curve of Fig. 11(b).

where $SS(j)$ is the smoothed sum of gray values in column j and span, the size of sliding window in filtering, is the only smoothing parameter. In this paper, we set span = 40. Fig. 11 shows the smoothed gray-value curve corresponding to Fig. 10 with span = 40. It can be seen that compared to original ones, the new gray-value curves appear to be smoother with noise point removed, which is conducive to feature extraction of the gray-value curves.

3) Range Judgement Based on the First-Order difference of Gray Values: A close look at Fig. 11 reveals that there are obvious differences between the gray-value curves of a weld fusion and a weld perforation. It is shown that the gray-value curve of weld perforation has much larger range than that of weld fusion, with more prominent curve peaks and valleys. Thus, in this paper, we propose to employ the first-order difference of the gray-value curve, which can appropriately reflect the amplitude of variation in the gray value, in order to distinguish between the two types of weld defects.

In a discrete function, the so-called first-order difference is the difference between two consecutively adjacent elements [33]. Mathematically, the first-order difference of $X(k)$ is given by $Y(k) = X(k+1) - X(k)$. As can be seen from Fig. 11, the difference in the gray values between the two adjacent points is to extract the features of the curve. Thus, in this paper, a

modified first-order difference method in which the first-order difference of the sum of gray values in each column is given by

$$d_j = s_{j+w} - s_j, j \in [1, n-w]. \quad (12)$$

Then, the first-order difference sequence of the gray values of weld defects can be obtained as

$$D = [d_1, \dots, d_j, \dots, d_n] \quad (13)$$

where w is the distance between the two elements. If the value of w is too small, the first-order difference cannot reflect sudden changes in gray values, namely the features of weld defects. On the contrary, if the value of w is too large, it may exceed the width of the defect area so that the variation of the gray value in the defect area cannot be detected at all. The issue of value selection for w will be addressed in detail in the following section. With the obtained sequence D , we can use its range R for distinguishing the two types of weld defects. Specifically, we have the following classification criterion:

$$R = \max(d_j) - \min(d_j), d_j \in D \quad (14)$$

$$\text{Flag} = \begin{cases} \text{Weld perforation,} & R \geq T_3 \\ \text{Weld fusion,} & R < T_3 \end{cases} \quad (15)$$

The value selection of T_3 depends on w and will also be discussed in the following section.

D. Weld Defect Classifier

Summarizing the earlier classification methods for weld defects, we propose the following decision tree classifier as shown in Fig. 12.

V. EXPERIMENTS AND DISCUSSIONS

A. Sampling Environment of Welding Seam and the Weld Defect Detection System

The earlier weld detection method was integrated into a real-time weld detection system used for actual production lines of metal canister welding. In this system, welding seams are photographed and detected in real-time. In order to ensure the stability of the system and the detection efficiency, the entire system equipment was fixed on the production line. The metal canisters welded in this production line are about 35 cm in length, the speed of welding is about 60 cans/min, and the transmission speed of the metal canisters on the production line is about 35 cm/s. The models of the camera, the lens, and the light sources, given in Table I, are used for the detection system, in order to adapt to the transmission speed and ensure that the whole weld seam of each canister can be inspected.

The image acquisition system, which is used to collect the images of weld seams, is a main part of the real-time weld defect detection system, consisting of a camera, lens, and light source. As Fig. 13(a) shows, in order to make the image shot clear and stable, the three devices and the weldment keep coaxial. Fig. 13(b) is the photograph of the weld defect detection system.

The structure of the whole real-time weld defect system is shown in Fig. 14. Besides, the weld defect system also includes

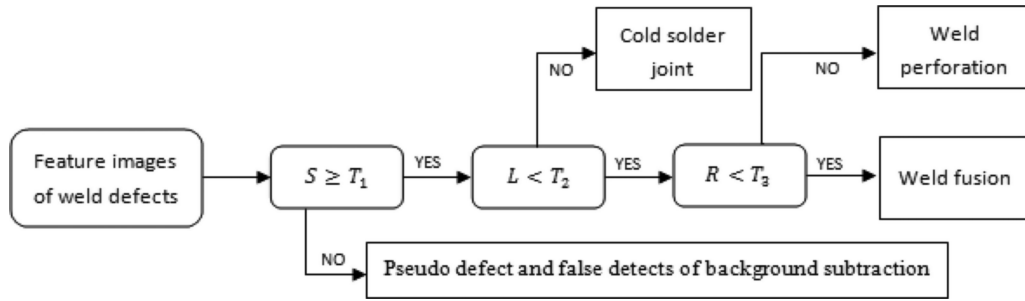


Fig. 12. Decision tree classifier for weld defects.

TABLE I
MODEL AND PARAMETERS OF IMAGE ACQUISITION EQUIPMENT

Equipment	Model	Parameters
Camera	AVT STINGAY F-125B/C, SONY CCD, ICX445	Size of target area is 4.8mm*3.6mm, imaging resolution is 1024*768, 15frames/s, shutter speed is 100μs.
Lens	Computar TEC-M55telecentric lens	Focus is 55mm, aperture is F32C, object distance is 300mm
Light source	Coaxial light source of Red LED LFV-34	Light intensity is set to the maximum

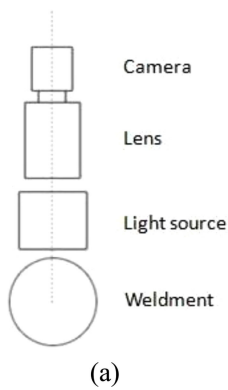


Fig. 13. (a) Hardware structure of the image acquisition system. (b) Photograph of the system.

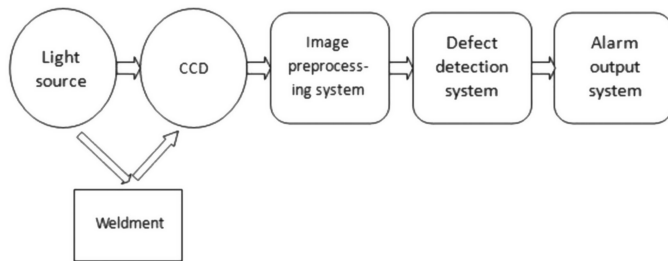


Fig. 14. Architecture of the real-time weld defect detection system.

the image processing system, the defect detection system, and the alarm output system. Here, the image preprocessing system is used to process the sampled images for the subsequent detection. The defect detection system is the core part of the whole system, including the OpenCV implementation the MBS algorithm and the weld defect classification algorithms. The alarm output system receives the detection signal from the defect detection system, pushing the defect canisters off from the

production line, and at the same time alarming and prompting the type of the weld defect.

The system runs on an industrial personal computer with a Pentium E5300 CPU 2.60 GHz processor with a 2 GB RAM and a Windows XP platform. In this configuration, the processing time of each weld seam image is about 30–35 ms. Since the shot frequency of the camera is 15 frames/s, a processing time less than 60 ms can meet the requirement of detection.

B. Comparison With the Classical Background Subtraction Algorithms

In our experiments, the MBS method we proposed in Section III was compared with the classical background subtraction algorithms as mentioned in Section I. We used all those five algorithms in our weld defect detection system to construct the backgrounds: SG [19], mixture of Gaussians (MOG) [20], KDE [21], subspace learning using PCA (SLPCA) [22], and the proposed MBS we proposed.

A total of 100 consecutive nondefective samples were used to build the background model in this experiment. When using SG, MOG, KDE, and MBS, their maximum iterations were all set to be 100, and the actual iteration numbers in algorithm executions were always lower than 100 in most cases. For the SLPCA method, we input all these 100 images to construct the background model. The computational time and iteration numbers costed to build a background are given in Table II. We also used 50 normal welds and 30 defective images to test the accuracy of each model.

It is shown in Table II that the method has a highest accuracy, followed by MOG, whose model is same as the method. However, with a different parameter update strategy, MOG needed more iterations and computational time than MBS. Using a simple model, the SG method consumed the least computational time and iterations among all the methods, but it yielded a low detection accuracy. The accuracy of KDE is not satisfactory

TABLE II
COMPARISON OF MBS WITH OTHER FOUR CLASSICAL ALGORITHMS

Algorithm	Iterations	Time	Right detections	Accuracy
SG	31	13s	49	61.25%
MOG	66	33s	69	86.25%
KDE	50	55s	56	70.00%
SLPCA	100	71s	42	52.50%
MBS	43	18s	76	95.00%

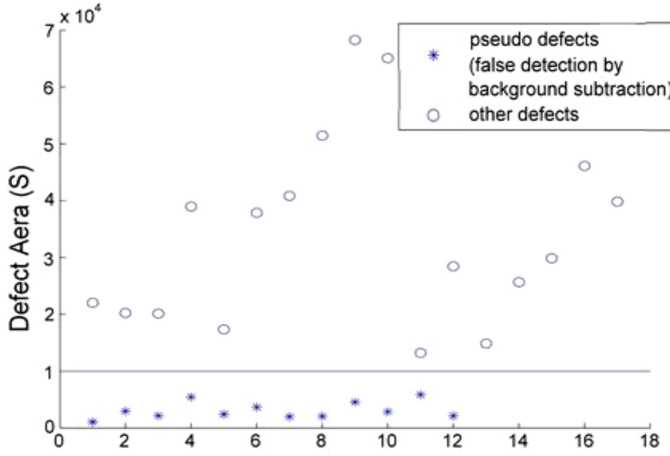


Fig. 15. Comparison of defect areas.

because, to some extent, this method is too sensitive to welding defects so that some normal weld seams were detected falsely. For SLPCA, a total of 100 sample images were not enough to construct a robust background, so its accuracy was the lowest. In conclusion, among all these algorithms, the method (MBS) is showed to the most suitable for welding defect detection for the thin-walled metal canister production.

C. Threshold for Defect Area Detection

Defect area detection is the first step in the detection and classification of weld defects. By calculating the feature area of the weld defects, the pseudoweld defects (or false detection by background subtraction) and genuine weld defects can be distinguished. As indicated in Section IV, T_1 in (5) can be obtained by comparing the areas of general weld defects and those of pseudodefects or false detections. In order to ensure the universality of the value of T_1 , a set of experiments were performed with the results shown in Fig. 16, which plots the areas of 17 genuine weld defects and the areas of 12 pseudodefects or false detection by background subtraction.

It is shown in Fig. 15 that the difference between the areas that are genuine weld defects and the pseudodefects (or false detects by background subtraction) is significant. We can further found that if we take $T_1 = 1 \times 10^4$ as the threshold of S in (7), the genuine weld defects can be well distinguished from pseudodefects or false detection by background subtraction. Although the value of T_1 varies with the width of weld seams, essentially with the production line, in this paper, we set $T_1 = 1 \times 10^4$ for our experiments.

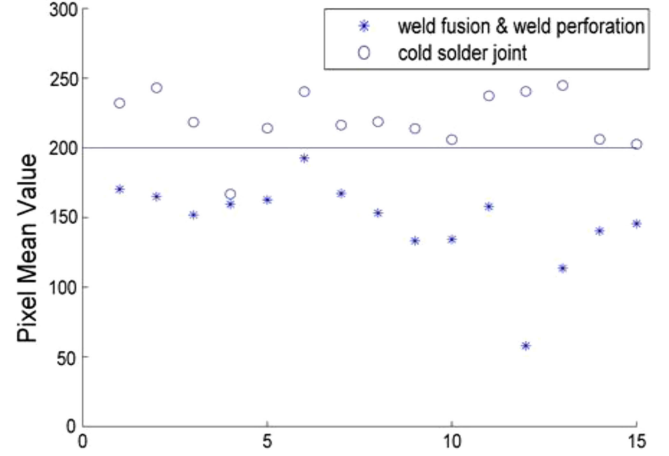


Fig. 16. Comparison of mean pixel values of weld fusions and weld perforations with colder solder.

D. Threshold for Defect Brightness Detection

After the defect area detection, cold solder joints can be distinguished from the other defects according to the mean pixel values of the weld defect areas. Fig. 16 shows the mean pixel values of 15 cold solder joints and those of 15 other two types of weld defects obtained by the image acquisition system. Except some samples, the mean pixel values of cold solder joint samples are larger than 200, while those of weld fusions or weld perforations are smaller than 200, implying that the two types of weld defects have significant difference in mean pixel values.

It can be seen that the pixel mean value of the exceptional sample is smaller than other cold solder joint samples. After analysis, we found that this exceptional sample was due to colder soldering and meanwhile some displacement of the weldment led to false detection by background subtraction. The mixture of the two weld features thus resulted in the reduced mean pixel value of the defect area. However, the probability of occurrence of such a case is very small in actual production, which has little influence on the detection results. As such, considering the usual cases, we take $T_2 = 200$ as the threshold for defect brightness detection.

E. Threshold for the First-Order Difference Method

As described in the following section, the value of T_3 in (15) is dependent on the value of w in (12), and both of them have great influence on the accuracy in the classification of weld fusions and weld perforation according to gray-value curves. Too large or too small value of w may result in unobvious distinction between the features of the weld fusion and the weld

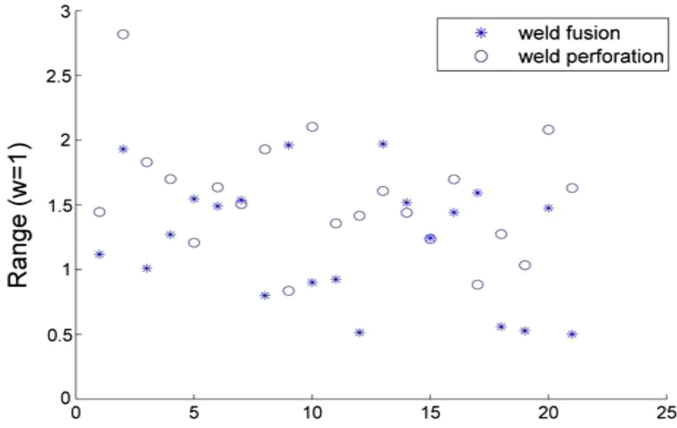


Fig. 17. Distribution of R when $w = 1$.

perforation, implying that it is difficult to appropriately select the value of T_3 in order to obtain satisfactory classification accuracy. Next, we will demonstrate the effectiveness of (12) and then investigate the relationship between w and the range R empirically, which can help us find appropriate values of w and T_3 .

If $w = 1$, (12) is essentially the traditional definition of first-order difference. Fig. 17 shows the distribution of range R when $w = 1$, plotting 21 samples of weld fusion and 21 samples of weld perforations. It can be observed that the range R 's of both weld fusions and weld perforations are mainly on the interval (0.5, 2.5) and there is little difference between the two types of weld defects, so that the value of T_3 in (15) cannot be determined when $w = 1$. This is why we propose (12) with $w > 1$, which can make the feature of gray-value curves more apparent.

In order to justify that the enlarged w can differentiate the ranges of gray values of weld fusions and weld perforations, we plotted the R - w relation diagrams of weld fusions and weld perforations with five different weld perforations and six different weld fusions in Fig. 18, respectively. For each individual curve in Fig. 18, the range R increases with the increasing w , as the overall trend. However, by comparing the R - w diagrams of the two types of weld defects, it can be revealed that the range R of weld perforation increases faster than that of weld fusion with the increasing w .

Except some samples, the ranges of most of the weld perforations begin to stabilize when w reaches 60. In contrast, the ranges of weld fusions increase more slowly, and most of them keep increasing when $w \in (0, 150)$. Thus, we can find that when $w = 60$, the difference between the ranges of the two types of weld defects are most apparent so that it is most easily to distinguish between the two types of weld defects.

With the appropriate value of w , we further determined the threshold T_3 with the given samples. Fig. 19 plots the ranges of the gray-value curves of 21 weld fusions and 21 weld perforation when $w = 60$. It shows that most of the points corresponding to the ranges of the two types of weld defects can be separated by the line $R = 53$. Thus, we select $w = 60$ for the distance of the first-order difference and $T_3 = 53$ for the threshold. It should be noted that these values of w and T_3 are selected with

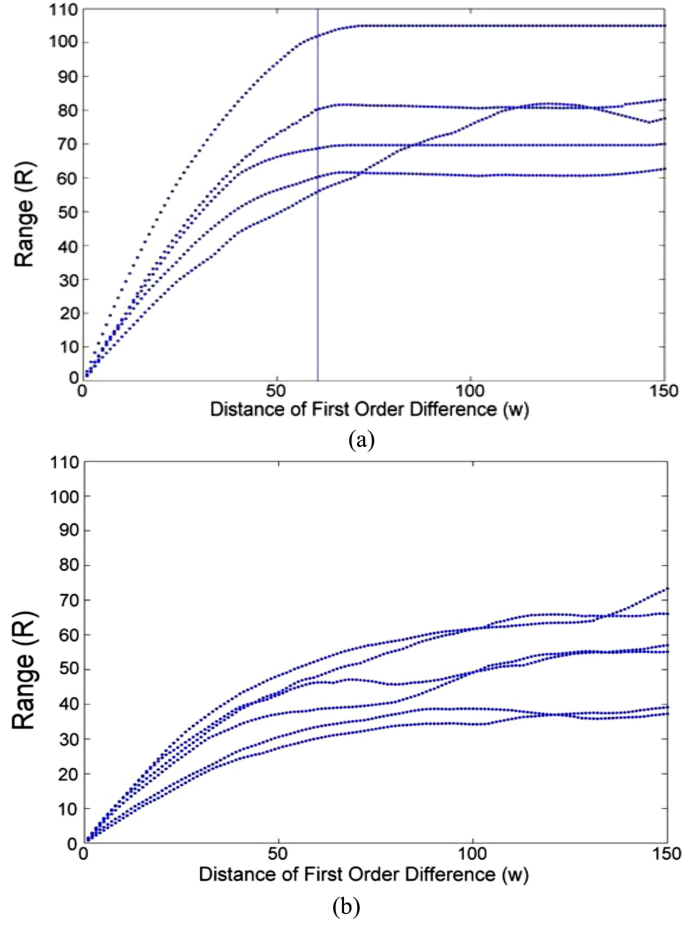


Fig. 18. (a) R - w diagram of weld perforations. (b) R - w diagram of weld fusions.

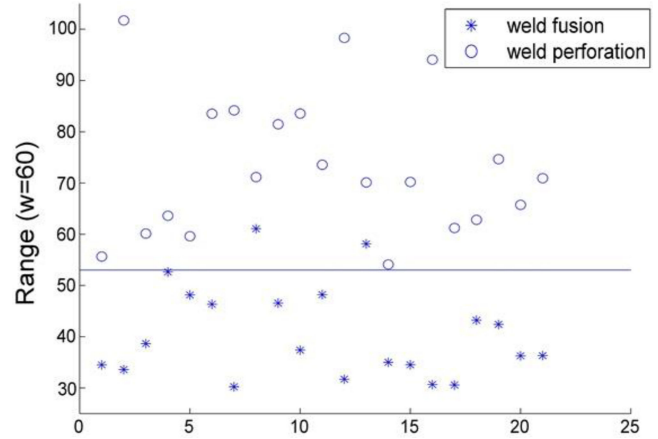


Fig. 19. Distribution of range R when $w = 60$.

the given parameters of the image acquisition system and the given production line. However, the above statistical method for determining their values is universally applicable to any configuration and any production line.

F. Results for Detection Experiments

Before the system works on the production line for real-time weld defect detection, we tested and evaluated the whole system,

TABLE III
EXPERIMENT DATA OF SIMULATED DETECTION

	Normal weld	Pseudo defects	Cold solder joints	Weld fusions	Weld perforations	Total
The number of samples	71	15	18	25	21	150
Proportion to total	40.66%	16.67%	12%	16.67%	14%	100%
The number of false detections	1	1	0	0	0	2
The number of missing detections	0	0	1	3	0	4
Accuracy rate	98.59%	93.33%	94.44%	88%	100%	96%

TABLE IV
EXPERIMENT DATA OF ACTUAL DETECTION

	Normal weld	Pseudo defects	Cold solder joints	Weld fusions	Weld perforations	Total
The number of cans	18970	92	46	17	15	19140
Proportion to total	99.11%	0.48%	0.24%	0.09%	0.08%	100%
The number of false detections	78	4	0	0	0	82
The number of missing detections	0	0	3	1	0	4
Accuracy rate	99.59%	95.65%	93.48%	94.12%	100%	99.55%

particularly the defect detection and classification algorithm by using the collected cans, some of which are with normal weld seams, and the other of which are with weld defects. The cans were put on the production line, moving through the image acquisition system, and being photographed by the system. In total, 150 pictures of welding seams were shot on the line with each detected by the algorithm of the weld defect system. These pictures contain three types of weld defects, pseudodefects, or normal welding seams. Table III lists the experimental results.

Of the 150 images of weld seams, there are 71 normal weld seams with one detected by mistake. A total of 15 images contain pseudodefects and one of them was detected falsely. For 18 cold solder joints, there were no false detections but one escaped detection. Besides, 3 of 25 weld fusions were undetected and 21 weld perforations were successfully detected. Overall, the detection algorithm reached an accuracy rate of 96%, with the false detection rate 1.3% and missing detection rate 2.7%. Therefore, the accuracy of the detection algorithm can be considered to be able to basically meet the requirements of actual production.

G. Weld Defect Detection in the Actual Production Line

After testing and evaluation of the detection algorithm, the system was then used for defect detection in the actual production of thin-walled metal canisters. After a one-week production period, the production line produced 19 140 canisters totally, including 78 defective cans and 92 products with pseudodefects (which were also all screened manually). Table IV lists the statistical results for detection.

It is shown that there 78 of 18 970 normal welds and 4 of 92 pseudodefects were detected by mistake. By observing the weld images of these falsely detected cans, we found that these weld images were blurred because of the vibration of the production line, or the position of the pseudodeflect are too close to the areas of the weld seams, which thus resulted in false detections. There were also some weld defects (1 cold solder joint and 3 weld fusions) escaping detection by the system. These defective welds are not apparent visually so that the feature

areas are small. Overall, the detection accuracy rate reached 99.55%, which meets the needs of the actual production.

VI. CONCLUSION

In this paper, we proposed an effective method of weld defect detection and classification for high-frequency resistance welding of thin-walled metal canisters, and designed and constructed a corresponding system for real-time weld defect detection on the production line. The core part of the system is the proposed weld defect detection and classification algorithm with the features of weld defect areas extracted by an MBS method based on a Gaussian mixture model. Particularly, we also proposed to use the range of the first-order difference of the sum of gray values in each column of the feature image for distinguishing between weld fusions and weld perforations. It was shown by the comparative experimental results and the detection results in the actual production line that the system armed with the proposed detection method cannot only effectively identify weld defects with high accuracy, but also can distinguish the types of weld defects accurately. Thus, the system can reduce labor costs for the factory significantly, and it can also help workers to adjust the production line timely in order to avoid defective products.

REFERENCES

- [1] N. P. Mahalik, "Processing and packaging automation systems: a review," *Sens. Instrum. Food Quality Safety*, vol. 3, no. 1, pp. 12–25, 2010.
- [2] I. Valavanis and D. Kosmopoulos, "Multiclass defect detection and classification in weld radiographic images using geometric and texture features," *Expert Syst. Appl.*, vol. 37, no. 12, pp. 7606–7614, 2010.
- [3] N. Nacereddine *et al.*, "Weld defect detection in industrial radiography based digital image processing," in *Proc. World Acad. Sci., Eng. Technol.*, vol. 2, 2005, pp. 145–148.
- [4] N. Boaretto and T. M. Centeno, "Automated detection of welding defects in pipelines from radiographic images DWDI," *NDT E Int.*, vol. 86, pp. 7–13, 2017.
- [5] B. Chen *et al.*, "Accurate defect detection via sparsity reconstruction for weld radiographs," *NDT E Int.*, vol. 94, pp. 62–69, 2018.
- [6] W. Hou, "Deep features based on a DCNN model for classifying imbalanced weld flaw types," *Measurement*, vol. 131, pp. 482–489, 2019.

- [7] M. Leo *et al.*, "Automatic visual monitoring of welding procedure in stainless steel kegs," *Opt. Lasers Eng.*, vol. 104, pp. 220–231, 2018.
- [8] L. Li *et al.*, "Welding quality monitoring of high frequency straight seam pipe based on image feature," *J. Mater. Process. Technol.*, vol. 246, pp. 285–290, 2017.
- [9] D. Ding, "Visual neural network model for welding deviation prediction based on weld pool centroid," *Int. J. Pattern Recognit. Artif. Intell.*, vol. 32, no. 8, 2018, Art. no. 1859014.
- [10] Y. Li *et al.*, "Measurement and defect detection of the weld bead based on online vision inspection," *IEEE Trans. Instrum. Meas.*, vol. 59, no. 7, pp. 1841–1849, Jul. 2010.
- [11] B.K. P. Horn and B. G. Schunck, "Determining optical flow," *Artif. Intell.*, vol. 17, no. 1–3, pp. 185–203, 1981.
- [12] S. M. Smith, "ASSET-2: Real time motion segmentation and shape tracking," in *Proc. 5th Int. Conf. Comput. Vis.*, 1995, pp. 237–244.
- [13] S. Panahi *et al.*, "Evaluation of background subtraction methods," in *Proc. Digit. Image Comput., Techn. Appl.*, 2008, pp. 357–364.
- [14] M. Weng, G. Huang, and X. Da, "A new interframe difference algorithm for moving target detection," in *Proc. 3rd Int. Congr. Image Signal Process.*, 2010, vol. 1, pp. 285–289.
- [15] M. Piccardi, "Background subtraction techniques: a review," in *Proc. IEEE Int. Conf. Syst., Man Cybern.*, 2004, vol. 4, pp. 3099–3104.
- [16] A. M. McIvor, "Background subtraction techniques," *Proc. Image Vis. Comput.*, vol. 4, pp. 3099–3104, 2000.
- [17] T. Horprasert, D. Harwood, and L. S. Davis, "A statistical approach for real-time robust background subtraction and shadow detection," presented at the IEEE Frame-Rate Appl. Workshop, Kerkyra, Greece, 1999.
- [18] T. Bouwmans, F. E. Baf, and B. Vachon, "Statistical background modeling for foreground detection: A survey," in *Handbook of Pattern Recognition and Computer Vision*. Singapore: World Scientific, 2010, pp. 181–199.
- [19] C. R. Wren *et al.*, "Pffinder: Real-time tracking of the human body," *IEEE Trans. Pattern Anal. Mach. Intell.*, vol. 19, no. 7, pp. 780–785, Jul. 1997.
- [20] C. Stauffer and W. E. L. Grimson, "Adaptive background mixture models for real-time tracking," in *Proc. IEEE Comput. Soc. Conf. Comput. Vis. Pattern Recognit.*, 1999, vol. 2, pp. 248–252.
- [21] M. A. Elgammal, D. Harwood, and L. S. Davis, "Non-parametric Model for Background Subtraction," in *Proc. Eur. Conf. Comput. Vis.*, 2000, pp. 751–767.
- [22] N. M. Oliver, B. Rosario, and A. P. Pentland, "A Bayesian computer vision system for modeling human interactions," *IEEE Trans. Pattern Anal. Mach. Intell.*, vol. 22, no. 8, pp. 255–272, Aug. 2000.
- [23] R. R. da Silva *et al.*, "Pattern recognition of weld defects detected by radiographic test," *NDT E Int.*, vol. 37, no. 6, pp. 461–470, 2004.
- [24] Y. Wang *et al.*, "Detection of line weld defects based on multiple thresholds and support vector machine," *NDT E Int.*, vol. 41, no. 7, pp. 517–524, 2008.
- [25] R. Vilar, J. Zapata, and R. Ruiz, "An automatic system of classification of weld defects in radiographic images," *NDT E Int.*, vol. 42, no. 5, pp. 467–476, 2009.
- [26] C. G. Windsor *et al.*, "The classification of weld defects from ultrasonic images: A neural network approach," *Brit. J. Non-Destruct. Test.*, vol. 35, no. 1, pp. 15–22, 1993.
- [27] Z. Zivkovic, "Improved adaptive Gaussian mixture model for background subtraction," in *Proc. Proc. 17th Int. Conf. Pattern Recognit.*, 2004, vol. 2, pp. 28–31.
- [28] J. C. S. Jacques, C. R. Jung, and S. R. Musse, "A background subtraction model adapted to illumination changes," in *Proc. Int. Conf. Image Process.*, 2006, pp. 1817–1820.
- [29] J. W. Davis and V. Sharma, "Robust background-subtraction for person detection in thermal imagery," in *Proc. Conf. Comput. Vis. Pattern Recognit. Workshop*, 2004, pp. 128–128.
- [30] O. Barnich and M. Van Droogenbroeck, "ViBe: A universal background subtraction algorithm for video sequences," *IEEE Trans. Image Process.*, vol. 20, no. 6, pp. 1709–1724, Jun. 2011.
- [31] J. Zhang and J. Hu, "Image segmentation based on 2D Otsu method with histogram analysis," in *Proc. Int. Conf. Comput. Sci. Softw. Eng.*, 2008, vol. 6, pp. 105–108.
- [32] I. Haritaoglu, D. Harwood, and L. S. Davis, "W 4: Real-time surveillance of people and their activities," *IEEE Trans. Pattern Anal. Mach. Intell.*, vol. 22, no. 8, pp. 809–830, Aug. 2000.
- [33] R. C. Gonzalez and R. E. Woods, "Digital image processing," *Nueva Jersey*, 2008.



Jun Sun (S'02–M'08) received the Ph.D. degree in control theory and engineering, and the M.Sc. in computer science and technology from Jiangnan University, Wuxi, China, in 2009 and 2003, respectively.

He is currently a Full Professor with the Department of Computer Science and Technology, Jiangnan University. He is the Vice Director with Jiangsu Provincial Engineering Laboratory of Pattern Recognition and Computational Intelligence. He has authored or coauthored more

than 150 papers in journals, conference proceedings and several books in the above areas. His research interests include computational intelligence, machine learning, and bioinformatics, among others.



Chao Li received the Bachelor's degree from Nanjing University of Information Science and Technology, Nanjing, China, in 2013 and the M.Sc. degree from Jiangnan University, Wuxi, China, in 2017, respectively, both in computer science and technology. He is currently working toward the Ph.D. degree in pattern recognition and intelligent systems at Jiangnan University.

His research interests include computational intelligence and computer vision with several published papers in some journals and conference

in the above areas.



Xiao-Jun Wu received the B.Sc. degree in mathematics from Nanjing Normal University, Nanjing, China, in 1991. He received the M.S. degree in 1996, and the Ph.D. degree in pattern recognition and intelligent systems in 2002, both from Nanjing University of Science and Technology, Nanjing, China. In 2006, he was with Jiangnan University, where he is currently a Professor. He has authored or coauthored more than 200 papers in his fields of research. From 2003 to 2004, he was a Visiting Researcher with the Centre for

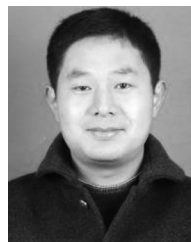
Vision, Speech, and Signal Processing, University of Surrey, Guildford, U.K. His current research interests include pattern recognition, computer vision, fuzzy systems, neural networks, and intelligent systems.



Vasile Palade (M'02–SM'04) received the Ph.D. degree from the University of Galati, Galați, Romania, in 1999.

Between 2004 and 2014, he was a Lecturer with the Department of Computer Science, University of Oxford, Oxford, U.K. He is currently a Reader in pervasive computing with the Faculty of Engineering, Environment and Computing, Coventry University, Coventry, U.K. He has authored or coauthored more than 100 papers in Journals and conference proceedings as well as

several books. His research interests include computational intelligence with application to bioinformatics, fault diagnosis, web usage mining, among others.



Wei Fang (M'15) received the Ph.D. degree in information technology and engineering of light industry from Jiangnan University, Wuxi, China, in 2008.

He is currently an Associate Professor of computer science with Jiangnan University. From 2013 to 2014, he was a Visiting Scholar with CEACIA, University of Birmingham, Birmingham, U.K. He has authored or coauthored more than 50 scientific papers in journals and international conferences. His current research

interests involve the evolutionary computation, swarm intelligence, multiobjective optimization, and large-scale global optimization.

Dr. Fang is currently an Editorial Board Member of several international journal.